LOW-ORDER AEROMECHANICS OF TILT-ROTOR HELICOPTERS

Wesley Appleton, Antonio Filippone and Nicholas Bojdo
University of Manchester, UK
wesley.appleton@manchester.ac.uk*

Abstract

The conversion corridor represents the safe region of flight for tilt-rotor aircraft during the transition bewteen helicopter and aeroplane mode. A low-order rotary-wing model has been established and validated throughout the conversion corridor, showing good agreement with experimental data. Furthermore, the equations of motion for longitudinal flight have been derived and solved to determine the conversion corridor boundaries with the results correlating well with published data. The largest discrepancy was observed at the lower boundary which indicated a downwash model of the rotor wake over the wing was required. Additionally, from a trimmed flight perspective, it was found the tilt-rotor aircraft had transitioned from helicopter to aeroplane mode by the approximate shaft angle $\gamma = 60°$.

1.   INTRODUCTION

Tilt-rotor helicopters operate as lateral-tandem, counter-rotating rotorcraft that combine rotary-wing and fixed-wing flight. This merges the flight envelopes of their respective counterparts and inherently allows these rotorcraft to fly faster and further than conventional helicopters, whilst losing none of their low speed and vertical/ short take-off and landing capabilities. These rotorcraft therefore fulfil an operational niche not shared by current in-service aircraft.

The transition between helicopter mode and aeroplane mode is known as the conversion corridor. It is a transient phase of flight that is both safety critical and mechanically complex. The conversion corridor, as shown in Figure 1, represents the upper and lower flight speed boundaries against the shaft angle. The boundaries are generally characterised by wing stall at the lower limit and installed engine power at the upper limit. During the transition between flight modes, the control

*Corresponding author email.

Copyright Statement

authority of the rotors are increased or decreased depending on the shaft angle and flight speed. Flying at intermediate shaft angles utilises a blend of fixed-wing and rotary-wing control mechanisms.
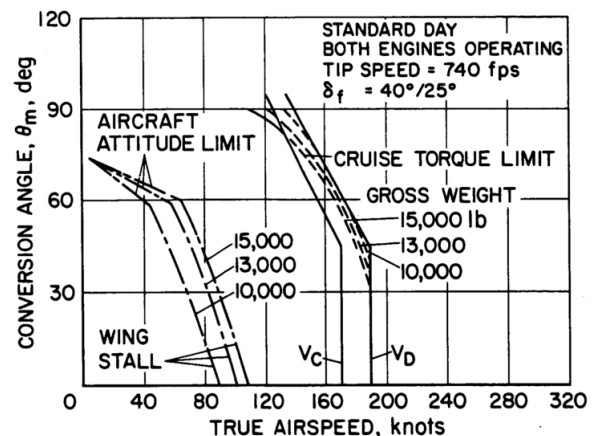

Figure 1: Bell XV-15 conversion corridor[1]

The construction of the conversion corridor requires the equations of motion to be solved at given shaft angles and flight speeds. To calculate the net forces and moments on the aircraft requires fixed-wing and rotary-wing aerodynamic models and additionally, a control authority model. Rotary-wing modelling is generally more computationally expensive than fixed-wing modelling due to several phenomena:

- Asymmetric lift due to a cyclic variation of the in-plane velocity.

- Reverse flow and dynamic stall on the retreating blade.

- Transonic Mach numbers and compressibility effects on the advancing blades.

- Periodic and/or unsteady aeroelastic blade deformations.

- Aerodynamic interferences, e.g. blade vortex interactions.

The use of low-order models are ideally suited for the design and assessment of tilt-rotor concepts and their conversion corridors. From the preliminary design stage, the rotor geometry is optimised for both helicopter and aeroplane mode. Furthermore, due to the tandem-rotor configuration several flight conditions (e.g. side-slipping flight or differential rotor control inputs) require separate evaluation of the induced velocity fields and blade dynamics to calculate the tandem-rotor performance. Therefore, validated low-order models which provide quick performance estimates that are sufficiently accurate are important in the preliminary design of tilt-rotor aircraft.

The work undertaken has derived the force and moment expressions for longitudinal flight (wings level and zero sideslip) for any generic tilt-rotor. Additionally, a low-order rotary-wing model has been established and validated against published experimental data. This model has been implemented into the equations of motion and the conversion corridor established based on a set of prescribed constraints. Furthermore, the trim states through the conversion corridor have been compared with published data and conclusions drawn with respect to general rotary-wing and fixed-wing behaviours.

2. AIRCRAFT MODEL

The aircraft model and aerodynamic analysis has been developed in dimensionless rotary-wing form: lengths are dimensionless with respect to the radius, R, and velocities with respect to shaft tip speed, ΩR. The force and moment vectors presented herein are dimensionless using the definitions:

$$(1) \quad \boldsymbol{F} = \frac{2\boldsymbol{F}^*}{\pi \rho \Omega^2 R^4},$$

$$(2) \quad \boldsymbol{G} = \frac{2\boldsymbol{G}^*}{\pi \rho \Omega^2 R^5},$$

where $\boldsymbol{F}^*$ and $\boldsymbol{G}^*$ are dimensional quantities and ρ is the air density (international standard atmosphere sea-level reference was used throughout). In the notation used, the rotor torque and power coefficients are identical. Data presented later will make use of this fact. Furthermore, all rotary-wing, fixed-wing and fuselage reference data, unless cited otherwise, was taken from Harendra et al. [2].

2.1. Coordinate Systems

In the proceeding analysis, several coordinate systems are introduced to simplify the modelling. All coordinate systems are Cartesian systems with the unit vectors $\boldsymbol{i}$, $\boldsymbol{j}$ and $\boldsymbol{k}$ subscripted with the appropriate frame of reference symbol. These are defined as follows:

1. Gravity system (subscript g): the conventional right-handed inertial coordinate system located at the aircraft centre of gravity (c.g.).

2. Body system (subscript b): the conventional right-handed coordinate system with the origin attached to the aircraft c.g..

3. Stability/ wind system (subscript w): the co-ordinate system aligned with the freestream wind vector. The system is co-located at the aircraft c.g. but rotated about the y_b-axis through the angle of attack, α, described by

$$(3) \quad T_{w \to b} = \begin{bmatrix} \cos\alpha & 0 & -\sin\alpha \\ 0 & 1 & 0 \\ \sin\alpha & 0 & \cos\alpha \end{bmatrix},$$

where the subscript arrow indicates the transformation direction. The angle of attack is defined by

$$(4) \quad \alpha = \tan^{-1}\frac{w}{u},$$

where u and w are the x_b- and z_b-axis components of the flight speed in the body frame. This transformation matrix is also used to transform the weight vector from the gravity system into the body system since the flight path angle is set to zero.

4. Shaft system (subscript s): is a non-rotating system describing the position of the rotor shaft relative to the body system. The shaft system is rotated about the y_b-axis through the shaft angle, γ. The shaft angle is defined to be $0°$ in aeroplane mode and $90°$ in helicopter mode.

The system is located at the centre of the rotor hub with the x_s-axis pointing parallel to the rotor shaft in the direction of conventionally positive thrust. The z_s-axis is positive towards the leading edge of the rotor disc and the y_s-axis makes a right-hand set. In aeroplane mode, the body and shaft axes are parallel but not necessarily coincident. A transformation from the body system to the shaft system is described

by

$$(5) \quad T_{b \to s} = \begin{bmatrix} \cos \gamma & 0 & -\sin \gamma \\ 0 & 1 & 0 \\ \sin \gamma & 0 & \cos \gamma \end{bmatrix} .$$

Alternatively, the shaft system velocity components can be computed directly from the wind vector if a shaft angle of attack, τ, is prescribed:

$$(6) \quad T_{w \to s} = \begin{bmatrix} \cos \tau & 0 & -\sin \tau \\ 0 & 1 & 0 \\ \sin \tau & 0 & \cos \tau \end{bmatrix} .$$

The shaft angle of attack is related to the shaft angle and body angle of attack through

$$(7) \quad \tau = \gamma + \alpha ,$$

and taken positive is the aft sense.

5. Blade system (subscript bl): is the rotating system attached to the rotor shaft. The system is coincident with the shaft system at the azimuth position $\psi = 90°$ on the advancing side of the rotor disc. The x_{bl}-axis is parallel to the shaft direction, the y_{bl}-axis runs along the blade span and the z_{bl}-axis makes a right-hand set. A transformation from the shaft system to the blade system is described by

$$(8) \quad T_{s \to bl} = \begin{bmatrix} 1 & 0 & 0 \\ 0 & \sin \psi & -\cos \psi \\ 0 & \cos \psi & \sin \psi \end{bmatrix} .$$

6. Flapping system (subscript f): is the rotating system attached to the flapping origin. The system is coincident with the blade system at zero flap angle and rotated about the z_{bl}-axis through the flap angle, β, positive conventionally 'upwards'. A transformation from the blade system to the flapping system is described by

$$(9) \quad T_{bl \to f} = \begin{bmatrix} 1 & -\beta & 0 \\ \beta & 1 & 0 \\ 0 & 0 & 1 \end{bmatrix} ,$$

where the small angle approximations $\sin \beta \approx \beta$ and $\cos \beta \approx 1$ have been made.

7. Blade wind system (subscript lw): is the reference system aligned with the resultant velocity normal to the leading edge of the blade element. The system involves a single rotation through the inflow angle, ϕ, defined by

$$(10) \quad \phi = \tan^{-1} \frac{V_P}{V_T} ,$$

where V_P and V_T are the perpendicular and tangential velocity components in the flapping frame. The blade element lift, drag and moment coefficients are defined in this reference frame and rotated back to the flapping frame through

$$(11) \quad T_{lw \to f} = \begin{bmatrix} \cos \phi & 0 & \sin \phi \\ 0 & 1 & 0 \\ -\sin \phi & 0 & \cos \phi \end{bmatrix} .$$

The existence of a velocity component along the blade span yaws the resultant velocity over a blade element by the angle

$$(12) \quad \chi = \sin^{-1} \frac{V_R}{\|\boldsymbol{V}_f\|} ,$$

where V_R is the radial velocity component and $\|\boldsymbol{V}_f\|$ denotes the Euclidean norm of the flapping velocity vector - the velocity magnitude. This resultant velocity is resolved through the cosine of the yaw angle to give the velocity normal to the leading edge of the blade.

2.2. Aircraft Discretisation

The aircraft model was based on the Bell XV-15 research tilt-rotor[1,2,3,4], but the methodology is applicable to general tilt-rotor aircraft. The aircraft was discretised into several parts: fuselage, rotors, wing and nacelle, and horizontal tail. The vertical tails were not included as the focus was on the longitudinal motion of the aircraft. These parts were analysed individually in their appropriate reference frame to determine their three-dimensional force and moment contributions. The aeromechanic quantities were then transformed into the body frame and summed to give the total forces and moments.

The position coordinates of several components, referenced from the aircraft c.g. at the aft limit are presented in Table 1. The longitudinal change in the c.g. position with shaft angle was assumed to be negligibly small. Furthermore, the longitudinal rotor hub position was determined from

$$(13) \quad x_b{}^R = x_b{}^P + l \cos \gamma ,$$

$$(14) \quad z_b{}^R = z_b{}^P - l \sin \gamma ,$$

where the superscript P denotes the pivot position and l is the dimensionless straight-line distance from the pivot to the rotor hub.

Table 1: Dimensionless reference distances from the c.g..

Component	x_b	y_b	z_b
Fuselage	0.05	0.00	-0.02
Starboard pivot	0.01	1.29	-0.12
Port pivot	0.01	-1.29	-0.12
Wing	0.06	0.00	-0.09
Horizontal tail	-1.73	0.00	-0.14

The work undertaken has focussed on the implementation of a rotary-wing model into the longitudinal equations of motion for tilt-rotor aircraft. Aerodynamic data relating to the fuselage, wing and horizontal tail was taken from lookup tables defined in the wind system. The data was converted into rotary-wing nomenclature by multiplying the data by the tip speed ratio, $J = V_\infty/(\Omega R)$, where V_∞ is the flight speed, and area ratio, $A = S/(\pi R^2)$, where S is the reference area of the fuselage, wing or horizontal tail. Lastly, aerodynamic data was corrected for compressibility using the extended Prandtl-Glauert expression

$$(15) \quad C = \frac{C_0}{\beta},$$

where C is the compressibility corrected C_0 and β is given by

$$(16) \quad \beta = \frac{A\!\!R + 4\cos\Lambda}{A\!\!R\sqrt{1 - M^2\cos^2\Lambda} + 4\cos\Lambda}.$$

The aspect ratio is denoted by $A\!\!R$, the wing sweep angle (positive aft) by Λ and M is the Mach number.

3. FLIGHT MECHANICS

The conversion corridor represents the combinations of shaft angle and flight speed that permit the aircraft to fly steady and trimmed. These trim points are defined by a solution to the equations of motion that does not break any constraints. Mathematically, steady and trimmed flight is defined by the vector x that satisfies $f(x) = 0$, where f is a vector function. In the work undertaken, only the longitudinal motion of the aircraft is considered and hence, the vector function is given by

$$(17) \quad f(x) = \begin{pmatrix} X_b(x) \\ Z_b(x) \\ M_b(x) \end{pmatrix},$$

where X_b and Z_b are the longitudinal force components along the x_b- and z_b-axes and M_b is the pitching moment about the y_b-axis.

The solution vector to the equations of motion is

$$(18) \quad x = \begin{pmatrix} \theta \\ \theta_0 \\ \theta_s \\ \eta \end{pmatrix},$$

where θ is the aircraft pitch angle (positive above the horizon), θ_0 is the rotor collective pitch, θ_s is the longitudinal cyclic pitch and η is the elevator deflection. Since there are four variables to solve three equations, the system of equations is underdetermined. To overcome this, the moment control variables θ_s and η are related to a single variable, ζ, to create a unique solution to the equations of motion:

$$(19) \quad \theta_s = f_1(\zeta),$$
$$(20) \quad \eta = f_2(\zeta).$$

The ζ variable can be considered as the longitudinal control stick displacement and f_1 and f_2 are arbitrary functions. Limits of $\zeta = \pm 1$ were set that represented the arbitrary control input limits, $\zeta = 1$ being the forward displacement to give a nose-down moment and $\zeta = -1$ being the aft displacement giving a nose-up moment. The longitudinal cyclic pitch and elevator deflection were related to the ζ stick displacement through

$$(21) \quad \theta_s = \frac{\mathrm{d}\theta_s}{\mathrm{d}\zeta}\zeta,$$
$$(22) \quad \eta = \frac{\mathrm{d}\eta}{\mathrm{d}\zeta}\zeta,$$

where $\frac{\mathrm{d}\theta_s}{\mathrm{d}\zeta}$ and $\frac{\mathrm{d}\eta}{\mathrm{d}\zeta}$ are the control derivatives. These derivatives were taken originally from Harendra et al.[2], however, their dependence on the dimensional stick displacement was removed. Additionally, the longitudinal cyclic was approximated using a sinusoidal wash-out with shaft angle. The control derivatives are then

$$(23) \quad \frac{\mathrm{d}\theta_s}{\mathrm{d}\zeta} = -10°\sin\gamma,$$
$$(24) \quad \frac{\mathrm{d}\eta}{\mathrm{d}\zeta} = 20°.$$

The elevator deflection was positive downwards and the negative longitudinal cyclic pitch gives the nose-down moment with respect to forward stick displacement. This closes the control problem and the solution vector to the equations of motion be-

comes

$$(25) \quad x = \begin{pmatrix} \theta \\ \theta_0 \\ \zeta \end{pmatrix} .$$

The net force and moment vectors on the aircraft were established from the discrete summation from several components. The rotary-wing aerodynamics were defined in the shaft system and the fuselage and fixed-wing aerodynamics in the stability/ wind system. The discrete contribution from each aircraft part was found by applying the kinematic relationships transforming the forces and moments into the body system:

$$(26) \quad \boldsymbol{F}_b = T_{x \to b} \boldsymbol{F}_x ,$$

$$(27) \quad \boldsymbol{G}_b = T_{x \to b} \boldsymbol{G}_x + \boldsymbol{p}_b \times \boldsymbol{F}_b ,$$

where $\boldsymbol{F}$ and $\boldsymbol{G}$ are force and moment vectors, the subscript x denotes the reference system in which the forces and moments are expressed (other than the body system), $\boldsymbol{p}$ is the position vector of the forces and $\boldsymbol{G}_x$ are moments expressed in frame x.

4. ROTARY-WING MODELLING

4.1. Blade Model

The XV-15 rotor blade geometry was taken from Felker et al.[5]. The blade implements five aerofoils from the NACA 64-series, although, only one has published experimental data. Instead, a similar blade was constructed using data from Abbot et al.[6]. A comparison of the blade aerofoils is given in Table 2. The aerodynamic data was tabulated for incompressible flow and at a single Reynolds number of $Re = 10^6$. The lookup table called the lift, drag and pitching moment coefficients as functions of the local angle of attack.

Table 2: Original and model aerofoils along the dimensionless blade span.

Position, r	Original	Model
0.09	NACA 64-935	NACA 64-618
0.17	NACA 64-528	NACA 64-418
0.51	NACA 64-118	NACA 64-218
0.80	NACA 64-(1.5)12	NACA 64-412
1.00	NACA 64-208	NACA 64-208

In each case, an attempt to match the thickness-to-chord ratio and design lift coefficient was made. The model blade implemented thinner aerofoil sections compared with the original blade before $r = 0.51$ and the design lift coefficients are generally

somewhat smaller along blade span (except at $r = 0.51$ and $r = 1.00$). As a result, some degree of discrepancy was expected between the experimental and theoretical results, especially in the stalled regions and the flapping response to collective and cyclic pitch inputs.

4.2. Stall Model

Aerodynamic data outside of the experimental angle of attack range was approximated using the trigonometric models suggested in Leishman[7]:

$$(28) \quad C_l = A \sin(2(\alpha - \alpha_0)) ,$$

$$(29) \quad C_d = B + C \cos(2(\alpha - \alpha_0)) ,$$

$$(30) \quad C_m = D \sin(\alpha - \alpha_0) + E \sin(2(\alpha - \alpha_0)) .$$

In the set of equations A, B, C, D and E are experimentally determined coefficients, α is the angle of attack and α_0 is the zero-lift angle of attack.

The empirical models suggested the values: $A = 1.175$, $B = 1.135$, $C = -1.050$, $D = -0.500$ and $E = 0.110$, based on experimental data from the NACA 0012 and SC1095 rotorcraft aerofoils. Both these aerofoils are relatively thin and stall is initiated from the leading edge; characterised by an abrupt loss of lift. By contrast, thicker aerofoils exhibit a trailing stall with a more gradual loss of lift. Therefore, the stall model was best suited for the outboard, thinner sections of the blade. As noted by Johnson[8], in helicopter mode the inboard sections of the highly twisted blades are stalled even for moderate thrusts. Consequently, the thin aerofoil stall model may fail to capture the inboard stall behaviour adequately. Nonetheless, the models were implemented to approximate stall and reverse flow aerodynamics.

4.2.1. Compressibility

In forward flight, the local Mach number on the advancing side of the rotor can become transonic. If the local Mach number exceeds the critical Mach number, supersonic flow exists in regions along the aerofoil chord. If the drag-divergence Mach number is reached, the drag force on the aerofoil section sharply increases and consequently, so does the required shaft power. The drag-divergence Mach number was estimated using the empirical equation

$$(31) \quad M_{dd} = K - \frac{t}{c} - \frac{|C_l|}{10} .$$

The drag-divergence number is denoted by M_{dd}, K is a technology factor ($K = 0.87$ for NACA 6-series aerofoils), t/c is the thickness-to-chord ratio and

$|C_l|$ is the absolute value of the lift coefficient. In regions where the drag-divergence Mach number was exceeded, an incremental drag force, ΔC_d, was added to account for the wave drag[9]:

$$(32) \quad \Delta C_d = 12.5(M - M_{dd})^3 \, .$$

The empirical drag correction was based on experimental data for a NACA 0012 aerofoil. Therefore, it will not accurately capture the drag-divergence of the substitute XV-15 aerofoils but serves as a simple approximation. No transonic compressibility effects were made to the lift and moment data.

Below the drag-divergence Mach number, the aerodynamic characteristics of each aerofoil were corrected using the Kármán-Tsien[10,11] compressibility correction up to the Mach number $M = 0.70$:

$$(33) \quad C = \frac{C_0}{\sqrt{1 - M^2} + \frac{C_0}{2}\left(\frac{M^2}{1 + \sqrt{1 - M^2}}\right)} \, ,$$

where M is the local Mach number and C is the compressibility corrected C_0.

4.3. Blade Element Velocity Kinematics

The aerodynamic analysis was undertaken in the rotating flapping system using a blade element methodology. The velocity of a given blade element was calculated using the general expression for a static shaft:

$$(34) \quad \boldsymbol{V}_f = T_{bl \to f}\big(T_{s \to bl}(T_{w \to s}\boldsymbol{V}_w + \boldsymbol{v}_i) \\ + \boldsymbol{\omega}_{bl} \times \boldsymbol{p}_{bl}\big) + \boldsymbol{\omega}_f \times \boldsymbol{p}_f \, ,$$

where $\boldsymbol{V}_w$ is the flight speed vector, $\boldsymbol{v}_i$ is the induced velocity vector defined in the shaft system, T is a transformation matrix, $\boldsymbol{\omega}$ is a rotational velocity vector, $\boldsymbol{p}$ is a position vector and the subscripts denote the reference frames. These dimensionless quantities are given by:

$$
\begin{array}{lll}
\boldsymbol{V}_w = J\boldsymbol{i}_w & \boldsymbol{\omega}_{bl} = 1\boldsymbol{i}_{bl} & \boldsymbol{p}_{bl} = r_{bl}\boldsymbol{j}_{bl} \\
\boldsymbol{v}_i = -\lambda_i \boldsymbol{i}_s & \boldsymbol{\omega}_f = -\beta'\boldsymbol{k}_f & \boldsymbol{p}_f = r_f\boldsymbol{j}_f
\end{array}
$$

where J is the tip speed ratio, λ_i is the induced inflow ratio, r is a radial position and β' is the blade flapping velocity with respect to the azimuth. The induced inflow ratio was defined negative as the velocity kinematics describe the motion of the blade relative to air. Based on the small flapping angle approximation, the radial position along the blade span is equivalent in both the flapping system and blade system.

Denoting the flapping frame velocity vector as $\boldsymbol{V}_f = V_P\boldsymbol{i}_f + V_R\boldsymbol{j}_f + V_T\boldsymbol{k}_f$ and performing the kinematics gives the scalar perpendicular, radial and tangential components as:

$$(35) \quad V_P = J(\sin\tau + \beta\cos\tau\cos\psi) - \lambda_i + r\beta' \, ,$$
$$(36) \quad V_R = \beta(J\sin\tau - \lambda_i) - J\cos\tau\cos\psi \, ,$$
$$(37) \quad V_T = J\cos\tau\sin\psi + r \, .$$

The existence of a non-zero radial velocity component yaws the resultant flow over the blade element through the angle χ. This radial flow component is analogous to a swept wing seeing a yawed oncoming flow. To correct the two-dimensional blade element theory for this three-dimensional effect, the velocity magnitude is resolved through the yaw angle. The velocity normal to the leading edge is then

$$(38) \quad V = ||\boldsymbol{V}_f|| \cos\chi \, .$$

The unknown quantities in the velocity kinematic equations are the induced inflow and flapping states. Methods to solve for these quantities are presented in the proceeding sections.

4.4. Induced Inflow

The induced inflow ratio (dimensionless induced velocity) was calculated using a localised blade element momentum theory[12,13]. The theory assumed that global characteristics hold on a local level; the induced inflow at the rotor disc plane was half the final downstream value. The theory was selected due to its simplicity to implement and inexpensiveness computationally. The localised construction was adopted to capture the radial induced inflow distribution at a given azimuth location. The equation was solved iteratively using an under-relaxed, successive substitution scheme:

$$(39) \quad \lambda_{i\,n+1} = (1 - \kappa)\lambda_{i\,n+1}^* + \kappa\lambda_{i\,n} \, ,$$

where κ is the under-relaxation factor used to improve the solution convergence and

$$(40) \quad \lambda_i^* = -\frac{\sigma V^2(C_l\cos\phi + C_d\sin\phi)}{8r\sqrt{J^2 + \lambda_i^2 - 2J\lambda_i\cos\tau}} \, .$$

The solidity ratio based on the local dimensionless chord is denoted by $\sigma = Nc/\pi$, where N is the number of blades, ϕ is the inflow angle and C_l and C_d are the lift and drag coefficients. Note, in the coordinate system used the drag force is *negative*.

The lift and drag coefficients were found from a lookup table based on the local angle of attack computed from

$$(41) \quad \alpha = \begin{cases} \theta - \phi & \text{if } 0 \le \phi \le 180° \\ \theta - \phi - 360° & \text{otherwise} \end{cases} \, ,$$

where θ is the blade pitch angle measured from the z_{bl}-axis. The four quadrant resolution of the inflow angle was used to give the blade angle of attack in the range $-180° \leq \alpha \leq 180°$. The blade pitch angle term comprised of the geometric twist angle, θ_{tw}, collective pitch input, θ_0, longitudinal cyclic pitch input, θ_s, and a kinematic pitch-flap coupling term, δ_3 [14]:

(42) $\quad \theta = \theta_{tw} + \theta_0 + \theta_s \sin \psi + \beta \tan \delta_3 \,.$

The lateral cyclic pitch was omitted because the rolling moments from each rotor cancel in longitudinally symmetric flight.

The under-relaxation factor was initially set to $\kappa = 0.5$ but was successively halved depending on the local convergence history:

(43) $\quad \kappa = \begin{cases} 0.5\kappa & \text{if} \quad \varepsilon \geq 0 \quad \text{and} \quad \kappa > 10^{-3} \\ \kappa & \text{otherwise} \end{cases} \,,$

where ε is the absolute error between iterations.

4.5. Three-Dimensional Flowfield Effects

The blade element equations assume that the aerodynamics along the blade can be adequately modelled in a two-dimensional flowfield. However, in the vicinity of the blade tip a three-dimensional flowfield exists and a loss of lift is observed. This 'tip-loss' was accounted for using an effective blade radius, B. The selected value of the effective radius was established by comparing theoretical and experimental data, described in Section 6.1. The aerodynamics of the blade sections outboard of the effective radius retained only the profile drag, $C_d = C_{d_0}$, and the lift was set to zero, $C_l = 0$. A similar loss of lift is observed at the blade root, however, since the dynamic pressure is substantially lower in this region, its influence was considered negligibly small.

4.6. Blade Flapping Dynamics

The equation of motion describing the flapping dynamics of a rotor blade attached to a static shaft and gimballed rotor hub is [15,16]

(44) $\quad \beta'' + v^2 \beta = (v^2 - 1)\beta_{pc} + \dfrac{\rho R^5 A}{2I_\beta} \,,$

where β'' is the azimuthal blade acceleration, v is the dimensionless natural frequency, β_{pc} is the blade precone angle, ρ is the air density, I_β is the blade inertia about the flapping axis and A is the dimensionless aerodynamic moment. The dimensionless natural frequency is given by

(45) $\quad v^2 = 1 + \dfrac{2K_\beta{}^*}{NI_\beta \Omega^2} \,,$

$K_\beta{}^*$ is the *dimensional* flapping spring stiffness.

The aerodynamic moment was calculated using blade element theory, giving

(46) $\quad A = \displaystyle\int_e^1 r c V^2 (C_l \cos \phi + C_d \sin \phi)\, \mathrm{d}r \,,$

where e is the blade offset from the rotor shaft and c is the dimensionless local blade chord. The equation cannot be solved analytically and was therefore solved numerically.

4.6.1. Flapping Spring Moment

The existence of a flapping spring creates a physical moment on the rotor hub. In the flapping frame, the dimensionless spring moment due to a spring extension $\beta - \beta_{pc}$ creates a restoring moment on the blade given by

(47) $\quad \boldsymbol{G}_f^\beta = K_\beta(\beta - \beta_{pc})\boldsymbol{k}_f \,,$

where K_β is the *dimensionless* spring stiffness (using the moment definition in Section 2). The average spring moment on the rotor hub during a single revolution is found by transforming the spring moment into the shaft frame and applying the azimuthal averaging operator

(48) $\quad \bar{f}(\psi) = \dfrac{N}{2\pi} \displaystyle\int_0^{2\pi} f(\psi)\, \mathrm{d}\psi \,,$

where $\bar{f}(\psi)$ is the azimuthal average of $f(\psi)$. Performing the afore mentioned gives the shaft frame spring moment vector as

(49) $\quad \boldsymbol{G}_s^\beta = \dfrac{N K_\beta}{2}(\beta_c \boldsymbol{j}_s + \beta_s \boldsymbol{k}_s) \,,$

where β_c and β_s are the first harmonic Fourier coefficients of the cosine and sine functions:

(50) $\quad \beta_c = \dfrac{1}{\pi} \displaystyle\int_0^{2\pi} \beta \cos \psi\, \mathrm{d}\psi \,,$

(51) $\quad \beta_s = \dfrac{1}{\pi} \displaystyle\int_0^{2\pi} \beta \sin \psi\, \mathrm{d}\psi \,.$

4.6.2. Numerical Blade Flapping Solutions

The flapping equation of motion cannot be solved analytically without making several simpli-

fying assumptions that are not applicable to tilt-rotors. In the current work, the flapping dynamics were initially solved using four different methods[15,17]. The solutions were then compared in terms of accuracy and speed to select the most appropriate solver throughout the conversion domain. The four methods implemented were:

1. Steady-state method
2. Modified Taylor series
3. 4th order Runge-Kutta
4. System of first-order ordinary differential equations (ODEs)

The numerical methods were implemented to solve the flapping dynamics at three flight conditions representative of a tilt-rotor aircraft: hover, high speed helicopter mode and low speed conversion mode. In each case, the transient flapping motion was allowed to decay until a steady-state solution converged.

It was found that all the solutions were concordant with each other, suggesting a reliable steady-state solution was reached. A slight phase shift was observed using the modified Taylor series but this disappeared with increased azimuthal resolution and, consequently, computational time. Therefore, the modified Taylor series method was not chosen as the flapping solver. The steady-state method was marginally slower than the modified Taylor series but quicker than the Runge-Kutta and ODE system methods. At higher forward speeds above approximately $J = 0.35$ (160kn) some solutions did not converge using the ODE system (this was also observed in Krishnan[17]). This problem was not encountered with the other methods. As a result, the steady-state method was selected as the flapping solver for all flight conditions due to its robustness, speed and accuracy.

4.7. Rotor Performance

Having solved for the steady-state blade flapping states and induced inflow ratio, the differential rotor loads were computed. The dimensionless flapping frame aerodynamic force vector was denoted by

(52) $\ \mathrm{d}\boldsymbol{F}_f = \mathrm{d}F_x \boldsymbol{i}_f + \mathrm{d}F_y \boldsymbol{j}_f + \mathrm{d}F_z \boldsymbol{k}_f$,

with scalar components:

(53) $\ \mathrm{d}F_x = \dfrac{\sigma}{2\pi} V^2 (C_l \cos\phi + C_d \sin\phi)\,\mathrm{d}r\,\mathrm{d}\psi$,

(54) $\ \mathrm{d}F_y = 0$,

(55) $\ \mathrm{d}F_z = \dfrac{\sigma}{2\pi} V^2 (C_d \cos\phi - C_l \sin\phi)\,\mathrm{d}r\,\mathrm{d}\psi$.

The flapping frame forces were then transformed into the shaft frame. Denoting the dimensionless differential shaft frame force vector by

(56) $\ \mathrm{d}\boldsymbol{F}_s = \mathrm{d}C_T \boldsymbol{i}_s + \mathrm{d}C_U \boldsymbol{j}_s + \mathrm{d}C_V \boldsymbol{k}_f$,

the scalar components were computed from

(57) $\ \mathrm{d}\boldsymbol{F}_s = T_{f\to s}\,\mathrm{d}\boldsymbol{F}_f$,

where $T_{f\to s}$ is the flapping frame to shaft frame transformation matrix, given by

(58) $\ T_{f\to s} = \begin{bmatrix} 1 & \beta & 0 \\ -\beta\sin\psi & \sin\psi & \cos\psi \\ \beta\cos\psi & -\cos\psi & \sin\psi \end{bmatrix}$.

The scalar contributions to the thrust, lateral and in-plane forces were then:

(59) $\ \mathrm{d}C_T = \mathrm{d}F_x + \beta\,\mathrm{d}F_y$,

(60) $\ \mathrm{d}C_U = \beta\,\mathrm{d}F_x \sin\psi + \mathrm{d}F_y \sin\psi + \mathrm{d}F_z \cos\psi$,

(61) $\ \mathrm{d}C_V = \beta\,\mathrm{d}F_x \cos\psi - \mathrm{d}F_y \cos\psi + \mathrm{d}F_z \sin\psi$.

The radial force term, $\mathrm{d}F_y$, although equal to zero in the current work, was retained for generalisation. Models accounting for the radial drag force can be found in the literature[15] but were not included in the present work. The total rotor force vector, $\boldsymbol{F}_s = C_T \boldsymbol{i}_s + C_U \boldsymbol{j}_s + C_V \boldsymbol{k}_s$, was then found by integrating along the blade radius and around the azimuth:

(62) $\ \boldsymbol{F}_s = \displaystyle\int_0^{2\pi} \int_e^1 \mathrm{d}\boldsymbol{F}_s$.

The total rotor moments, $\boldsymbol{G}_s = C_Q \boldsymbol{i}_s + C_R \boldsymbol{j}_s + C_S \boldsymbol{k}_s$, were calculated by summing the contributions from the aerodynamic loads, $\boldsymbol{G}_s^A$, and the flapping spring moments, $\boldsymbol{G}_s^\beta$:

(63) $\ \boldsymbol{G}_s = \boldsymbol{G}_s^A + \boldsymbol{G}_s^\beta$.

The differential aerodynamic loads were calculated from

(64) $\ \mathrm{d}\boldsymbol{G}_s^A = \left(T_{f\to s}\mathrm{d}\boldsymbol{G}_f^0\right) + \left(T_{f\to s}\boldsymbol{p}_f\right) \times \mathrm{d}\boldsymbol{F}_s$,

where $\mathrm{d}\boldsymbol{G}_f^0$ is the aerofoil pitching moment vector. The aerofoil pitching moment was $\mathrm{d}\boldsymbol{G}_f^0 = \mathrm{d}C_M \boldsymbol{j}_f$, where

(65) $\ \mathrm{d}C_M = \dfrac{\sigma}{2\pi} c V^2 C_m\,\mathrm{d}r\,\mathrm{d}\psi$.

Denoting the differential aerodynamic moment vector by

(66) $\ \mathrm{d}\boldsymbol{G}_s^A = \mathrm{d}C_Q^A \boldsymbol{i}_s + \mathrm{d}C_R^A \boldsymbol{j}_s + \mathrm{d}C_S^A \boldsymbol{k}_s$,

the scalar components were computed as:

(67) $\mathrm{d}C_Q^A = r\,\mathrm{d}C_V \sin\psi + r\,\mathrm{d}C_U \cos\psi + \beta\,\mathrm{d}C_M$,

(68) $\mathrm{d}C_R^A = -r\,\mathrm{d}C_T \cos\psi - \beta r\,\mathrm{d}C_V + \mathrm{d}C_M \sin\psi$,

(69) $\mathrm{d}C_S^A = \beta r\,\mathrm{d}C_U - r\,\mathrm{d}C_T \sin\psi - \mathrm{d}C_M \cos\psi$.

The total aerodynamic moment was again found by integrating along the blade radius and around the rotor azimuth:

(70) $\displaystyle \boldsymbol{G}_s^A = \int_0^{2\pi} \int_e^1 \mathrm{d}\boldsymbol{G}_s^A$.

The steady-state spring moment on the rotor hub (Equation 49) was summed with the integrated aerodynamic moments to give the total moments on the rotor hub.

4.8. Tandem Rotor Aerodynamics

Tilt-rotor aircraft operate as lateral-tandem helicopters. In longitudinally symmetric flight, the total rotor forces and moments in the body frame are related to a single rotor performance through:

(71) $\boldsymbol{F}_b^{L+R} = M_1 \boldsymbol{F}_b^{L|R}$,

(72) $\boldsymbol{G}_b^{L+R} = M_2 \left(T_{s\to b} \boldsymbol{G}_s^{L|R} + \boldsymbol{p}_b^{L|R} \times \boldsymbol{F}_b^{L|R} \right)$.

The superscripts $L+R$ (left and right) and $L|R$ are the combined performance and single rotor performance respectively, and M_1 and M_2 are the diagonal matrices $M_1 = \mathrm{diag}(2\ \ 0\ \ 2)$ and $M_2 = \mathrm{diag}(0\ \ 2\ \ 0)$. These diagonal matrices double the longitudinal contributions and cancel the lateral contributions from each rotor.

5. CONVERSION CORRIDOR

5.1. Methodology

It was assumed that throughout the conversion corridor, a solution to the equations of motion existed that was finite and continuous. The conversion boundaries were determined using a sweep-and-refine methodology. The sweep was started from a shaft angle of $\gamma = 90°$ (helicopter mode) and flight speed of 0kn (hover). At the initial shaft angle and sequentially increasing flight speeds, an attempt to solve the equations of motions was made. Upon an interval where a solution and no viable solution was found (i.e a solution that broke constraints), the velocity interval was bisected until the appropriate lower or upper boundary was located. Having solved for the lower and upper boundaries

at a given shaft angle, at the subsequent shaft angles a further attempt was made to solve the equations of motion at the previous flight speed boundaries. If no viable solution was found, the velocity was incremented by 20kn and the same procedure followed to determine the boundaries.

Having located the conversion corridor boundaries at a given shaft angle, the flight speed range was divided into several discrete flight speeds and the equations of motion were solved. This was done to investigate how the steady and trimmed solutions changed with flight speed and shaft angle, and ensure no constraints were broken between the flight speed boundaries.

The equations of motion represented a system of nonlinear equations which were solved using a multivariate Newton-Raphson iteration scheme described by

(73) $\boldsymbol{x}_{n+1} = \boldsymbol{x}_n + J(\boldsymbol{x}_n)^{-1} \boldsymbol{f}(\boldsymbol{x}_n)$,

where J, in this instance, is the Jacobian matrix of partial first-order derivatives:

(74) $J = \begin{bmatrix} X_\theta & X_{\theta_0} & X_\zeta \\ Z_\theta & Z_{\theta_0} & Z_\zeta \\ M_\theta & M_{\theta_0} & M_\zeta \end{bmatrix}$.

These derivatives were approximated using a forward finite-difference scheme, e.g.

(75) $X_\theta = \dfrac{X(\theta + h) - X(\theta)}{h}$,

where h is some arbitrary increment in the derivative variable.

Most systems of nonlinear equations require an initial guess close to the solution vector to converge. During the conversion corridor, the collective pitch varies by as much as $30°$ to ensure the rotor does not stall. Therefore, no single initial guess of the collective pitch was sufficient to be used throughout the conversion. The relationship

(76) $2C_T = (C_{mg} - C_{d_0}{}^F) \sin\gamma + C_{d_0}{}^F$,

where C_{mg} was the weight coefficient and $C_{d_0}{}^F$ was the profile drag coefficient of the fuselage, was established to estimate an initial collective pitch setting. The fuselage profile drag was assumed to be $C_{d_0}^F = 0.05(J^2/3)$ (J^2 converts the fixed-wing coefficient into rotary-wing form and the fuselage area ratio was assumed to be $1/3$). Since the thrust produced is largely independent of the tip path plane angle of attack[14], the rotor performance was analysed without inclusion of the flapping dynamics to reduce computation time. In the first instance, the

initial guess was then

$$(77) \quad x_0 = \begin{pmatrix} 0 \\ \theta_0{}^* \\ 0 \end{pmatrix} ,$$

where $\theta_0{}^*$ is the collective pitch that satisfied Equation 76.

If the system of equations was solved at a particular flight speed, the solution vector became the initial guess for the subsequent flight speed. If no solution was found at this flight speed, another attempt was made to solve the equations of motion using Equation 77.

5.2. Conversion Corridor Constraints

The conversion corridor boundaries were determined from solutions to the equations of motion that did not break the prescribed performance constraints. These constraints ensured the steady shaft power, flapping angle and control limits were not exceeded:

1. Steady shaft power (single rotor)[3]: $\frac{C_P}{\sigma} \leq 0.033$
2. Flapping limit[2,3]: $|\beta| \leq 12°$
3. Control limit: $|\zeta| \leq 1$

No structural or pitch attitude constraints were imposed.

The conversion corridor presented was calculated for an aircraft mass of 5900kg (13000lbs), a shaft tip Mach number of $M_{stip} = 0.65$, flaperon setting of $\delta_f = 40°/25°$ and c.g. in the aft position (see Table 1).

6. RESULTS AND DISCUSSION

6.1. Rotary-Wing Model Validation

The predicted rotor performance has been assessed in terms of the thrust and power coefficients, figure of merit and propulsive efficiency. The figure of merit, FM, and propulsive efficiency, η, are defined by:

$$(78) \quad FM = -\frac{C_T{}^{3/2}}{2C_P} ,$$

$$(79) \quad \eta = -\frac{JC_T}{C_P} .$$

6.2. Axisymmetric Inflow

The validation cases for axisymmetric inflow for three different effective radii are presented in Figures 2 and 3. The results show the model predicts

the figure of merit and propulsive efficiency relatively well in each case. In hover, the figure of merit is best matched using the effective radius $B = 0.95$, although is somewhat invariant in aeroplane mode. The slightly smaller effective radius compared with general helicopter literature ($B = 0.97$) is accounted for by the higher disc-loading for tilt-rotor helicopters. Consequently, strong tip vortices create a larger region of three-dimensional flow and tip-region losses.
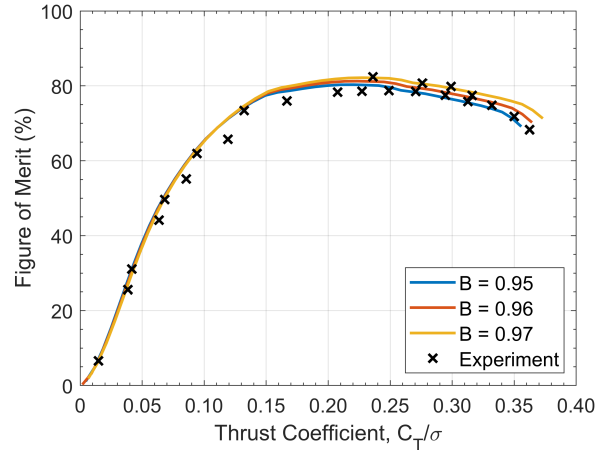
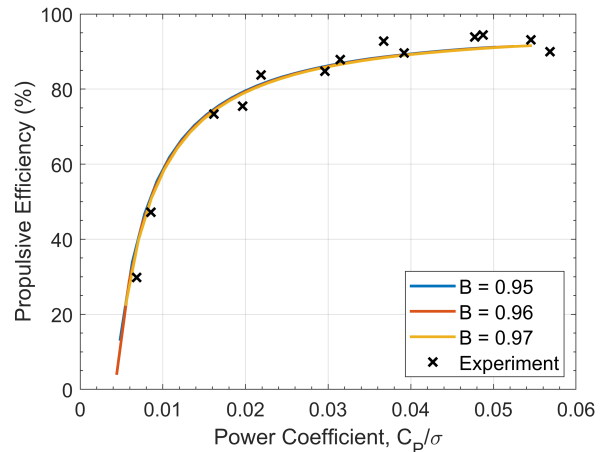Figure 2: Predicted and measured[5] figure of merit against thrust for different effective radii.

Figure 3: Predicted and measured[18] propulsive efficiency against shaft power for different effective radii.

6.3. Asymmetric Inflow

The validation cases for asymmetric inflow in helicopter and conversion mode are presented in Figures 4 and 5. The results show that the model adequately predicts the required shaft power for any

given thrust setting. However, the model does under predict the shaft power at high thrust settings in helicopter mode. Additionally, in conversion mode, the model continually over predicts shaft power. These discrepancies are accounted for by differences in the aerodynamic data and deficiencies in the stall and drag-divergence models.
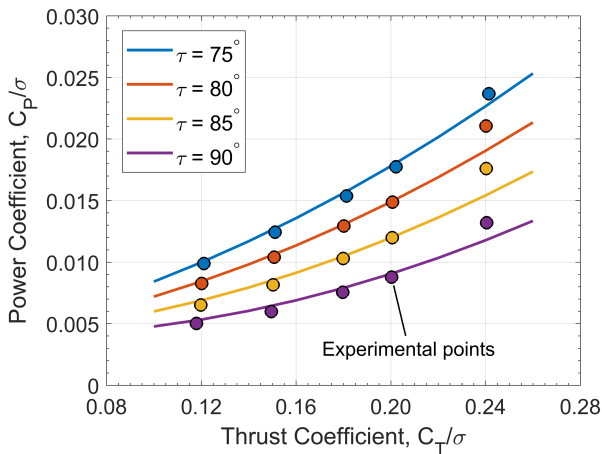

Figure 4: Predicted and measured[19] shaft power vs. thrust for several shaft angle of attacks in helicopter mode at a tip speed ratio $J = 0.17$.
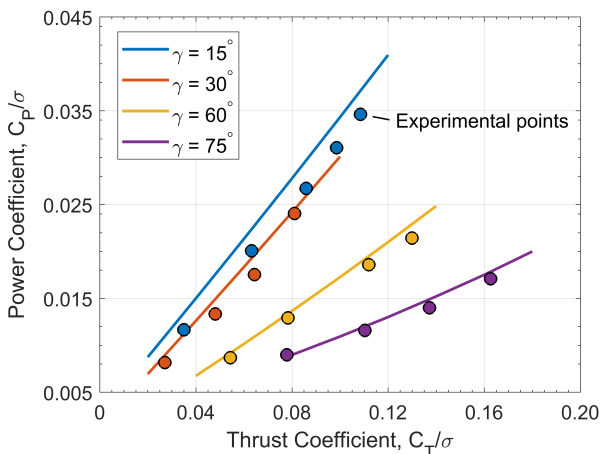

Figure 5: Predicted and measured[8] shaft power vs. thrust for several shaft angles at a tip speed ratio $J = 0.32$.

More validation cases have been undertaken with the results giving similar accuracy, but only a handful have been presented. Owing to the differences between the original and model blade, a more rigorous assessment using an identical blade should be compared with comprehensive experimental data encompassing the entire flight envelope. Overall, the validation cases show the rotary-wing model captures the rotor performance to a level of accuracy sufficient for preliminary design purposes through the conversion corridor.

6.4. Conversion Corridor

Theoretically predicted and published conversion corridors are presented in Figure 6. Overall, the predicted conversion corridor showed good agreement to that presented in Maisel et al.[1]. The upper boundary was accurately predicted between the shaft angles $\gamma = 90°$ and $\gamma = 45°$. However, below the a shaft angle $\gamma = 45°$ the boundary was continually over predicted. The vertical line from the published corridor was a structural constraint and therefore overlooked in the absence of any structural considerations. Nonetheless, the general trend was consistent in the fact there was a steady increase of the upper flight speed boundary below the shaft angle $\gamma = 45°$. At the lower boundary, the wing stall was consistently over predicted, except in aeroplane mode. This implied the theoretical pitch attitude to trim was under predicted.
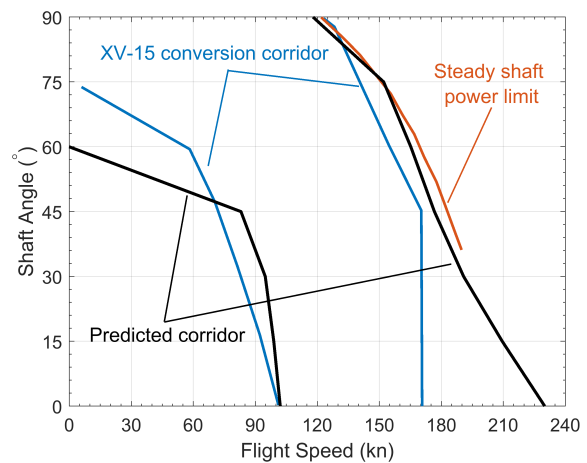

Figure 6: Calculated conversion corridor boundaries against the published conversion corridor[1].

The predicted trimmed pitch attitudes through the conversion corridor are shown in Figure 7, alongside comparative data from Harendra et al.[2]. The pitch attitude curves followed the expected trend whereby for a given shaft angle, as the flight speed increased a larger nose-down attitude was required. Lower flight speeds required a greater nose-up attitude to increase the magnitude of the wing lift vector or align the rotor thrust vector against the gravity vector. Thereafter, as the flight speed increased, a progressively greater nose-down attitude was observed to reduce the wing angle of attack and magnitude of the wing lift. Overall, the correlation of predicted pitch attitude agreed well with the published data for all shaft angles. There

was a consistent under prediction of pitch attitude but this was accounted for by the absence of any downwash models for both the rotor wake on the wing, and also the rotor and wing wake downwash over the horizontal tail.
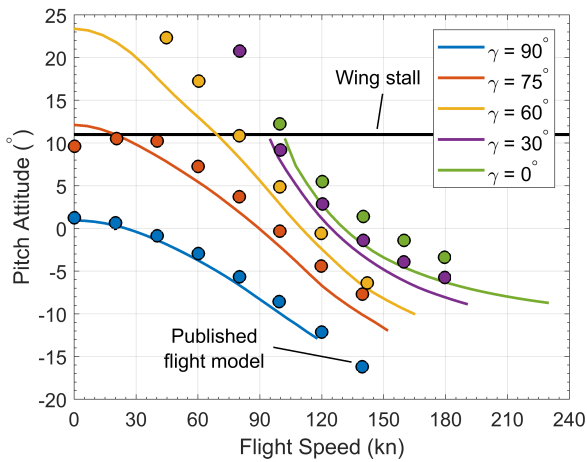

Figure 7: Predicted trimmed pitch attitude during the conversion corridor against data published in[2].

Helicopters typically transition into forward flight by pitching the aircraft nose-down to create lift and propulsive forces as components of the rotor thrust. This is usually done in a concave manner consistent with the shaft angles $\gamma = 90°$ and $\gamma = 75°$ in Figure 7. However, the trimmed pitch attitude against flight speed for a fixed-wing aircraft is usually a convex function, seen by the shaft angles $\gamma = 30°$ and $\gamma = 0°$ curves. Figure 7 therefore demonstrates the transition from helicopter to aeroplane mode, in terms of the adopted trimmed pitch attitude, is achieved early in the conversion corridor at approximately the shaft angle $\gamma = 60°$, where the curvature inflects.

The trimmed shaft power through the conversion corridor is shown in Figure 8. Additionally, the ζ control through the conversion corridor is shown in Figure 9. This shows that at a shaft angles $\gamma = 90°$ and $\gamma = 45°$, the limiting flight speed was actually constrained by the ζ control limit and not the engine power. This was attributed to differences in the flapping dynamics response to cyclic pitch inputs being under predicted, i.e. more cyclic pitch was required to achieve a desired tip path plane tilt. At all other shaft angles, the limiting constraint at the upper boundary was the engine power.

In the published literature, the lower conversion boundary was defined by the pitch attitude at the onset of wing stall, approximately $\theta = 11°$ with the inclusion of the wing setting angle of $\eta = 3°$. In the theoretical model, no limitation was made that the wing may not be stalled. The predicted lower
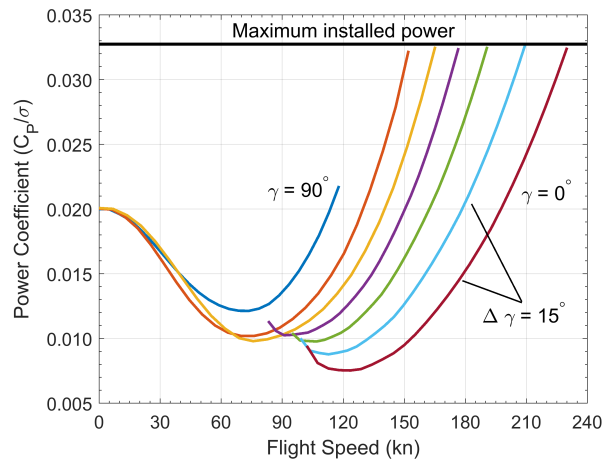

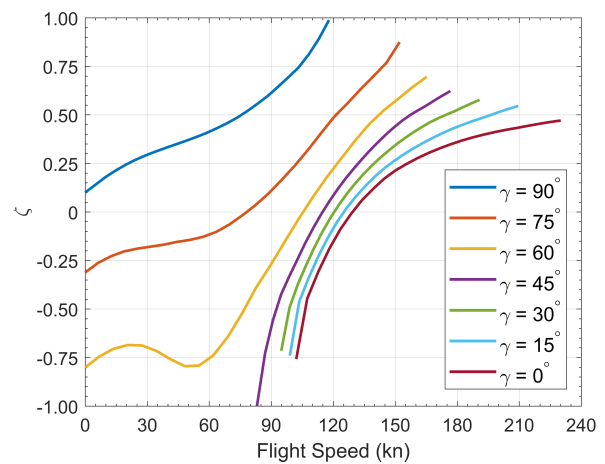Figure 8: Trimmed shaft power at several shaft angles, plotted for shaft increments of $\Delta\gamma = 15°$.

Figure 9: ζ control during the conversion corridor.

boundary for hovering flight was then observed to be $\gamma = 60°$, which was approximately $15°$ lower than the published corridor.

At this trimmed setting, the aircraft was pitched nose-up and the tip path plane tilted in the aft direction to align the thrust vector towards the gravity vector. This orientation would have caused significant interaction of the rotor wake over the wing, resulting in a download force and a pitch down moment. Therefore, additional aft tilt of the tip path plane would have been required to trim. As a result, the flapping constraint may have been broken and thus to accurately determine the lower conversion boundary a rotor wake downwash model is required.

The theoretical shaft power as a fraction of the maximum take-off power is compared in Figure 10. This shows that the required power was consistently under predicted through the corridor. In low-speed helicopter mode, the under prediction was

accounted for by the neglect of download. The measured download on the aircraft due to the rotor wake on the wing has been measured empirically at approximately 10% of the rotor thrust[20,21,22,23]. From Section 6.1, the rotor shaft power was reasonably well predicted over the full conversion corridor - under predicted at high thrust settings in helicopter mode and over predicted towards aeroplane mode. Therefore, the under predicted power through the conversion corridor was determined to result from an under predicted thrust requirement (and hence aircraft drag) due to the aerodynamic interactions from the rotor wakes and wing wake over the length of the aircraft. Furthermore, no rotor performance validation has been undertaken for negative shaft angles of attack and some discrepancy may exist in this region.
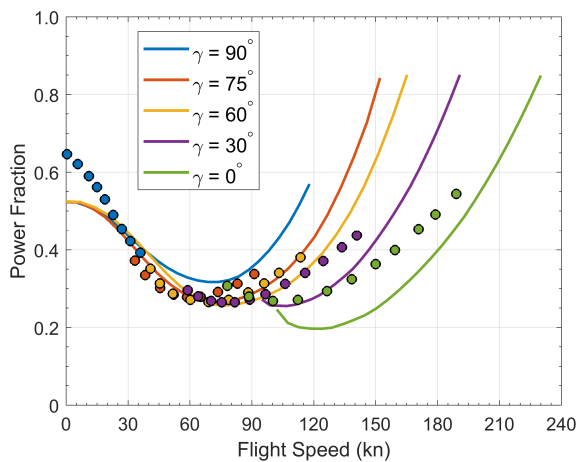

Figure 10: Comparison between the required and maximum power through the conversion corridor.

7. CONCLUSIONS

A low-order rotary-wing model has been developed and implemented into the equations of motion to solve the conversion corridor boundaries of tilt-rotor helicopters. The rotary-wing model displayed good agreement with experimental data throughout the conversion - under predicting the shaft power at high thrusts in helicopter mode and slightly over predicting the shaft power during conversion. This was determined to be from inaccuracies within the blade, stall and drag-divergence models. Additionally, the experimental data was best matched using an effective blade radius smaller than in conventional helicopter literature. Overall, the correlation between theoretical and experimental data indicates a level of accuracy suitable for preliminary design analysis and validates the implementation of low-order methods.

The conversion corridor boundaries were determined by solving the derived set of equations for longitudinal motion in a sweep-and-refine methodology. A set of prescribed constraints ensured the stalled engine power, flapping and control limits were not exceeded. A comparison between the theoretical and published conversion corridor showed a good level of accuracy.

The lower boundary was consistently over predicted leading to the conclusion that downwash models from the rotor wake and wing were required to improve the accuracy of the model. Between the shaft angles of $\gamma = 90°$ and $\gamma = 45°$ the upper boundary was well predicted and constrained mostly by the required shaft power. At a shaft angle $\gamma = 90°$, the upper boundary was constrained by the control limit. This was considered to arise from an over prediction of the cyclic pitch to generate the required tip path plane tilt when compared to the original blade model. At all other shaft angles, the upper boundary was constrained by the required shaft power. Below the shaft angle $\gamma = 45°$, the published corridor was limited by a structural constraint. In the developed model, no structural considerations were made and therefore the upper boundary in this region was over predicted.

From a steady and trimmed perspective, it was observed that the transition between helicopter mode and aeroplane mode was at the approximate shaft angle $\gamma = 60°$. Above this shaft angle, the trimmed pitch attitude solution to the equations of motion displayed a convex curvature; gradually pitching the aircraft nose-down to create lift and propulsive forces from the rotor thrust. Below a shaft angle $\gamma = 60°$, the curvature of the pitch attitude solutions inflected, demonstrating a trend of a fixed-wing nature.

The required power as a fraction of the total installed power was under predicted throughout the corridor. In low speed helicopter mode, this was accredited to the additional power required to compensate for the download force produced on the airframe from the rotor wake. However, in forward flight at higher speeds, the rotor wake is convected over the wing and the download effects are significantly reduced/ negligible. Since the rotor power was well predicted throughout the conversion corridor, it was concluded that the aircraft drag force was under predicted. This could have arisen from deficiencies in the airframe model, or neglect of any aerodynamic interference along the fuselage length (rotor and wing wake over the horizontal tail). Moreover, the rotor performance was not validated at negative shaft angles of attack and therefore an under predicted shaft power may have contributed to the total under predicted power when operating at

these inflow conditions.

ACKNOWLEDGEMENTS

REFERENCES

[1] M. Maisel, D. Borgman, and D. Few, "Tilt Rotor Research Aircraft Familiarization Document," *NASA Technical Memorandum X-62, 407*, 1975.

[2] P. Harendra, M. Joglekar, T. Gaffey, and R. Marr, "V/STOL Tilt Rotor Study - Volume V: A Mathematical Model For Real Time Flight Simulation of the Bell Model 301 Tilt Rotor Research Aircraft," *Bell Helicopter Company Report No. 301-099-001*, 1973.

[3] S. Ferguson, "A Mathematical Model for Real Time Flight Simulation of a Generic Tilt-Rotor Aircraft," *NASA Contractor Report CR-166563*, 1988.

[4] M. Maisel, D. Giulianetti, and D. Dugan, "The History of The XV-15 Tilt Rotor Research Aircraft: From Concept to Flight," *NASA Special Publication 4517*, 2000.

[5] F. Felker, M. Betzina, and D. Signor, "Performance and Loads Data from a Hover Test of a Full-Scale XV-15 Rotor," *NASA Technical Memorandum 86833*, 1985.

[6] I. Abbott, A. von Doenhoff, and L. Stivers Jr., "Summary of Aerofoil Data," *NACA Report No. 824*, 1945.

[7] G. Leishman, *Principles of Helicoter Aerodynamics*. Cambridge University Press, 2nd ed., 2006.

[8] W. Johnson, "An Assessment of the Capability to Calculate Tilting Prop-Rotor Aircraft Performance, Loads and Stability," *NASA Technical Paper 2291*, 1984.

[9] R. Prouty, *Helicopter Performance, Stability, and Control*. Florida: Kriger Publishing Company, 1st ed., 1989.

[10] H. Tsien, "Two-Dimensional Subsonic Flow of Compressible Fluids," *Journal of the Aeronautical Sciences*, vol. 6, no. 10, pp. 399–407, 1939.

[11] T. von Karman, "Compressibility Effects in Aerodynamics," *Journal of the Aeronautical Sciences*, vol. 8, no. 9, pp. 337–356, 1941.

[12] G. Padfield, *Helicopter Flight Dynamics*. Blackwell Publishing, 2nd ed., 2007.

[13] M. Heene, *Aerodynamic Propeller Model for Load Analysis*. Masters thesis, 2012.

[14] A. Bramwell, G. Done, and D. Balmford, *Helicopter Dynamics*. 2nd ed., 2000.

[15] W. Johnson, *Helicopter Theory*. Dover Publications, 1st ed., 1994.

[16] W. Johnson, *Rotorcraft Aeromechanics*. Cambridge University Press, 1st ed., 2013.

[17] V. Krishnan, *Aerodynamic and Performance Analysis of a Morphing Helicopter Rotor System*. Masters thesis, Embry-Riddle Aeronautical University, 2017.

[18] Bell Helicopters, "Advancement of Proprotor Technology. Task 2 - Wind-Tunnel Test Results," *NASA Contractor Report CR-114363*, 1971.

[19] M. Betzina, "Rotor Performance of an Isolated Full-Scale XV-15 Tiltrotor in Helicopter Mode," *American Helicopter Society Aerodynamics, Acoustics, and Test and Evaluation Technical Specialists Meeting*, pp. 1–12, 2002.

[20] R. Marr, K. Sambell, and G. Neal, "V/STOL Tilt Rotor Study. Volume VI: Hover, Low Speed and Conversion Tests of a Tilt Rotor Aeroelastic Model," *NASA Contractor Report CR-114615*, pp. 1–27, 1973.

[21] R. Marr, D. Ford, and S. Ferguson, "Analysis of the Wind Tunnel Test of a Tilt Rotor Power Force Model," *NASA Contractor Report CR-137529*, 1974.

[22] W. McCroskey, P. Spalart, G. Laub, M. Maisel, and B. Maskew, "Airloads on Bluff Bodies, with Application to the Rotor-Induced Downloads on Tilt-Rotor Aircraft," *NASA Technical Memorandoum 84401*, 1983.

[23] A. Desopper, O. Heuzé, V. Routhieau, S. Baehrel, G. Roth, and W. von Grünhagen, "Study of the Low Speed Characteristics of a Tiltrotor," pp. 1–14, 2002.